Heliyon 10 (2024) e40496

Contents lists available at ScienceDirect

Heliyon

journal homepage: www.cell.com/heliyon

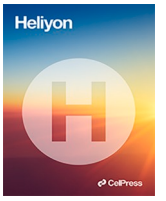

Research article

Post-correctional improvement of T2-weighted fast spin echo magnetic resonance imaging pulse sequence for detecting high intensity focused ultrasound thermal lesions

Gabrielle S. Lee [a,*], Graham A. Ferrier [a], Jahangir (Jahan) Tavakkoli [a,b]

[a] *Department of Physics, Toronto Metropolitan University, 350 Victoria Street, Toronto, ON, Canada*
[b] *Institute for Biomedical Engineering, Science and Technology (iBEST), Keenan Research Centre for Biomedical Science, St. Michael's Hospital, 209 Victoria Street, Toronto, ON, Canada*

ARTICLE INFO

Keywords:
High intensity focused ultrasound (HIFU)
Thermal ablation
Magnetic resonance imaging (MRI)
T2-weighted
Fast spin echo
Postprocessing
ex vivo model

ABSTRACT

High intensity focused ultrasound (HIFU) is a non-invasive therapy that induces heat in a small, localized volume of cancerous tissue without damaging neighbouring vital structures and cells. Precise targeting and treatment monitoring is typically achieved by pairing HIFU with an imaging modality such as magnetic resonance imaging (MRI). The most commonly used MRI pulse sequence for detecting HIFU thermal lesions is the T2-weighted fast spin echo (T2W-FSE) pulse sequence as it provides good contrast between normal and coagulated tissue. The drawbacks of the T2W-FSE pulse sequence are the manifestation of ringing artifacts and the loss of spatial resolution due to the signal modulation in k-space caused by the T2 decay. The inverse Fourier transform (IFT) multiplication scheme aims to remove the signal modulation by incorporating an inverse filter, which is an inverse of the signal modulation trend present in the k-space, to reduce the effects of T2 decay and improve image quality. In this study, four inverse filters (named as regular, narrow, wide, and compound) were developed and implemented on T2W-FSE MR images of *ex vivo* porcine muscle tissue with HIFU induced thermal lesion using a 0.55 T benchtop MRI research system (Pure Devices, Rimpar, Germany). Offline processing and enhancement of MR images of *ex vivo* porcine muscle tissue with HIFU induced thermal lesion using the narrow filter yielded the largest improvements of 13.8 ± 2.5 %, 17.0± 2.3 %, and 14.4± 1.1 % in lateral and axial spatial resolutions, and lesion signal-to-noise ratio (SNR), respectively, compared to the original images. Our results indicate an amplification of the signals in k-space and a reduction in the exponential signal modulation caused by T2 decay. These results also indicate the potential of the IFT multiplication scheme as an image processing method to improve thermal lesion detectability in MR-guided HIFU procedures.

1. Introduction

Approximately two in five Canadians are diagnosed with cancer during their lifetimes [1] and are usually treated by a combination of surgery, chemotherapy, and radiation therapy [2]. Thermal therapy is a minimally or non-invasive alternative cancer treatment that uses heat to destroy cancer cells without damaging adjacent vital structures and cells [3,4]. Thermal ablation is a type of thermal

* Corresponding author.
E-mail address: gabrielle.lee@torontomu.ca (G.S. Lee).

https://doi.org/10.1016/j.heliyon.2024.e40496
Received 23 July 2024; Received in revised form 14 November 2024; Accepted 15 November 2024
Available online 16 November 2024

therapy which involves increasing the tissue temperature to above 50 °C to destroy cancer cells [3]. Examples of minimally invasive thermal therapy modalities are radiofrequency (RF), microwave (MW), and laser because they require the percutaneous insertion of probes into the target tissue [3]. A more favourable non-invasive thermal therapy is high intensity focused ultrasound (HIFU), which focuses sound waves into a small focal region inside the body where the intensity at the focal point becomes high enough to raise the temperature above 50 °C and induce therapeutic effects [3]. This is typically achieved by placing a spherically concave ultrasound transducer, which has an impedance matching layer on its surface, along with coupling gel applied to the skin surface, ensuring efficient transmission of sound waves into the body [3].

Image guidance is fundamental in thermal therapy to ensure accurate targeting of the region-of-interest (ROI) as well as for treatment monitoring [5]. Ultrasound and magnetic resonance imaging (MRI) are two common imaging modalities used for precise targeting and treatment monitoring of HIFU procedures [6]. Compared with ultrasound, MRI has better spatial resolution and provides higher quality images of bone and soft tissue [7]. In addition, MRI utilizes a quantitative tissue thermometry method that can enhance the control and monitoring of HIFU thermal therapy [8].

T2-weighted fast spin echo (T2W-FSE) is the most widely used MRI pulse sequence to detect thermal lesions as it provides good lesion contrast in a short acquisition time [9,10]. However, the limitations of this pulse sequence are the manifestation of blurring or ringing artifacts and the loss of spatial resolution due to the signal modulation in *k*-space caused by the T2 decay [11]. Specifically, the T2 decay results in an exponential decrease in the MR signal after each 180 ° RF pulse [12], yielding a stairlike weighting function in *k*-space [13,14].

The discontinuity and exponential decay of the resulting stairlike weighting function cause ringing artifacts and a loss of spatial resolution in T2W-FSE MR images, respectively [11–14]. Although the T2 decay occurs in both the readout and the phase-encoding directions, the effect of T2 decay in the readout direction is negligible because the readout time is significantly shorter compared to the time between the first and last echo in the T2W-FSE pulse sequence [15]. Hence, the ringing artifacts and spatial resolution loss occur primarily in the phase-encoding direction [16].

With this understanding, a correction method was developed to remove ringing artifacts and improve the loss of spatial resolution caused by the T2 decay [15]. The method involves multiplying a filter function and a step exponential function to the phase-encoding direction to remove the discontinuity and decay of signals in *k*-space [15]. The successful application of the correction method by Zhou et al. in removing ringing artifacts and improving the spatial resolutions of MR images of water phantoms [15] has motivated this study toward using the correction method on MR images of *ex vivo* tissues with HIFU induced thermal lesions.

Although the research is grounded in an established method, which primarily focused on MR microscopy [15], we have developed and implemented a more simplistic method aimed at MR-guided thermal therapy procedures, as simpler and more efficient methods are more likely to be translated into clinical practice due to their ease of implementation and compatibility with existing workflows. The primary distinction between the previously established method and our method lies in its simplicity. Our method uses only an exponential function and involves fewer steps to reduce the effects of T2 decay. Additionally, MR images were optimized prior to implementing our method to further explore opportunities for image quality enhancement. In contrast, parameters in the established method were deliberately set to produce images with poor resolution and artifacts. Lastly, a quantitative image analysis was performed on MR images using image quality metrics to determine improvements in thermal lesion detectability and the successful implementation of this study will result in an enhanced MR imaging technique for the detection of HIFU thermal lesions in tissue.

2. Materials and methods

2.1. HIFU heating of ex vivo porcine muscle tissue

Porcine muscle tissue is frequently used in research as a substitute for human tissue due to its close anatomical and physiological similarities [17]. In this study, fresh *ex vivo* porcine muscle tissue acquired from a local grocery store was submerged in degassed water

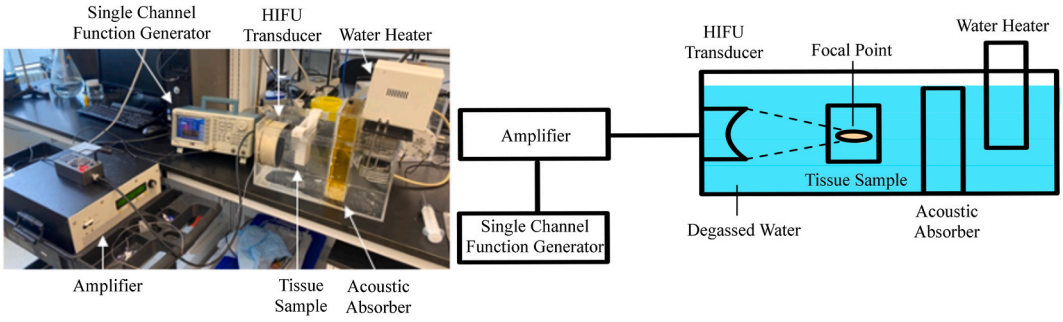

Fig. 1. Experimental setup for high intensity focused ultrasound (HIFU) heating of *ex vivo* porcine muscle tissue (left panel: picture, right panel: block diagram). A single channel function generator is connected to a radiofrequency (RF) amplifier to drive the HIFU transducer. The resulting focused ultrasound field propagates through water and a tissue sample to a focal point within the sample. The tissue sample was submerged in degassed water that was maintained at a clinically relevant temperature (37 °C) using a water heater. An acoustic absorber is placed behind the tissue sample to minimize acoustic reflections.

for 12 h in a 4 °C fridge to remove its gas content. The degassed *ex vivo* porcine muscle tissue was cut into samples of 7 cm × 7 cm × 3 cm (length × width × thickness) and was placed in a heated water bath (Neslab, Newington, NH, USA) at 37 °C for an hour to maintain a clinically relevant temperature.

The acrylic water tank used for this experiment contained a HIFU transducer (Imasonic, Voray sur l'Ognon, France) mounted on its sidewall to direct focused ultrasound energy horizontally into the tank (Fig. 1). Once the water tank was filled with degassed water, which was heated to 37 °C using a water heater (Thermo Fisher Scientific, Waltham, MA, USA), a 3D printed sample holder containing the tissue sample was submerged in the water tank to align the centre of the tissue sample with the focal point of the HIFU transducer. Inside the water tank, an acoustic absorber was placed behind the sample holder to minimize acoustic reflections from the opposite side wall of the tank.

The HIFU transducer was a single element therapeutic transducer with a centre frequency of 1 MHz and a focal length and aperture diameter of 100 mm and 125 mm, respectively. A single-channel function generator (AFG3101; Tektronix, Beaverton, OR, USA) and an impedance matching circuit delivered a 275 mV peak-to-peak (mV_{pp}) input voltage to the HIFU transducer for heating *ex vivo* porcine muscle tissue. In burst mode, the 1-MHz input pulses were delivered as 1000-cycle bursts at a 50 % duty cycle for 30 s and amplified using a radio frequency (RF) amplifier (AG1012; T&C Power Conversion, Inc., Rochester, NY, USA). The load power, which is forward power minus reflected power, was determined by connecting the function generator and amplifier in continuous mode to a 50 Ω dummy load, an electrical device that simulates an electrical load and safely dissipates the load power energy as heat.

In this configuration, a 77 W load power measured by the amplifier represented the maximum power delivered to the HIFU transducer. Therefore, the effective load power was 38.5-W at a 50 % duty cycle. In addition, since the efficiency in converting electric power to acoustic power was 63.9 % [18], the output acoustic power of the HIFU transducer was 24.6 W. This focused acoustic power generated thermal lesions in four tissue samples. An acoustics computational model developed in COMSOL Multiphysics (COMSOL Multiphysics, Stockholm, Sweden) simulated this HIFU heating, yielding an average lesion temperature of 56 °C. Lesioned tissues were cut into 6 mm diameter samples and imaged one-by-one while inside the 10 mm diameter bore of a benchtop MRI research system (Pure Devices, Rimpar, Germany). The MRI system consisted of a control unit and a permanent magnet operating with a static magnetic field strength of 0.55 T. The imaging parameters of the T2W-FSE pulse sequence were eight echo train lengths (ETL) with 36 averages for a 128 × 128 matrix at an echo time (TE) of 6 ms and a slice thickness of 3.5 mm. Here, ETL is the number of 180° pulses in a T2W-FSE pulse sequence [12], and TE is the time between the RF pulse and the peak of the MR signal [19]. Subsequently, a correction method was implemented, and a quantitative image analysis was performed to assess its improvement in image quality, as will be described in the next section.

2.2. Implementation of IFT multiplication scheme

Our correction method, also known as the inverse Fourier transform (IFT) multiplication scheme is a two-step process: 1) in the phase-encoding direction of *k*-space, we multiply an inverse filter, which represents the inverse of the exponential signal modulation caused by T2 decay, to the signal modulation itself (Fig. 2), and 2) apply a 2D IFT to the resultant signal to produce enhanced MR images. The exponential T2 decay causes a loss of signal modulation near the periphery of *k*-space (Fig. 2a), thereby worsening spatial resolution [15]. Therefore, multiplying the signal modulation by an inverse function should improve spatial resolution while preserving image contrast near the centre of *k*-space. The inverse filter was derived by taking the inverse of the signal modulation, resulting in exponential growth functions starting from the centre of *k*-space (Fig. 2b). Multiplying the inverse filter in the phase-encoding direction of *k*-space mitigates the exponential signal modulation (Fig. 2c).

In practice, the amplitude limits of the inverse filter (1–3, Fig. 3b) are arbitrarily set above the range of the measured signal modulation in *k*-space (0.1–0.7, Fig. 2a). The lower limit occurs at the centre of *k*-space, which determines the contrast of MR images [20]. A value of 1 ensured that the centre of the resultant *k*-space (Fig. 3b) remained unchanged after multiplication. Note that choosing a lower limit below 1 would decrease the signal in the centre of *k*-space, resulting in reduced contrast. The upper limit occurs at the periphery of *k*-space, which determines the spatial resolution of the image [20]. Although a high upper limit increases spatial resolution, it also increases the image noise level because the inverse filter amplifies both the signal and the noise [15]. After images

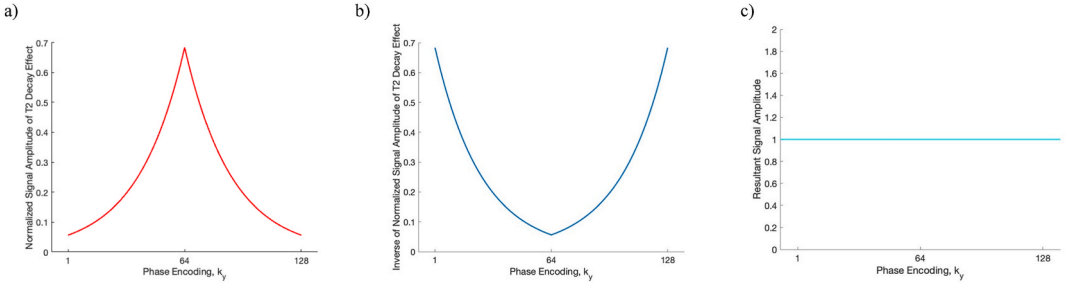

Fig. 2. Inverse Fourier transform (IFT) multiplication scheme. (a) The signal modulation in *k*-space was measured, exhibiting an exponential decay of signals in the phase-encoding direction of *k*-space caused by T2 decay. (b) The inverse of the signal loss - the inverse filter - was derived for each line in the frequency encoding direction of *k*-space. (c) The IFT multiplication scheme effectively mitigated the signal modulation observed in the phase-encoding direction of *k*-space.

were captured at various upper limits, it was determined that 3 was an optimal upper limit for our study due to the inherent trade-off between spatial resolution and signal-to-noise ratio (SNR).

The inverse of normalized signal decay caused by T2 decay, S, was curve fit to an exponential function in the phase-encoding direction in k-space (k_y) to determine its amplitude, C, and width, a, while $\beta = 1$:

$$S = C \cdot \exp^{\pm \beta a(-k_y)} \tag{1}$$

where Equation (1) is our proposed inverse filter. Optimization of S required finding a filter width that maximally amplified the signals and eliminating the exponential decay of signals in k-space caused by T2 decay. Three filter widths (Fig. 3b) were evaluated: *regular* ($\beta = 1$), *narrow* ($\beta = 0.5$), and *wide* ($\beta = 2$). In addition, since compounding techniques are frequently used to reduce speckle image noise [21], a compound filter was made by taking the k-spaces multiplied by all three filters (regular, narrow, and wide) individually and averaging them into a single k-space. Fig. 3c shows the resultant k-space after implementing the IFT multiplication scheme using various widths of the inverse filter. A 2D IFT was subsequently applied to yield the original T2W-FSE MR images as well as MR images enhanced by IFT multiplication scheme.

In summary, our IFT multiplication scheme consists of two steps: 1) multiplying the IFT multiplication filter – the inverse of the signal loss caused by T2 decay – to k-space, and 2) applying a 2D IFT to produce MR images. Fig. 4 is a flowchart of the IFT multiplication scheme.

2.3. Quantitative image analysis

A quantitative image analysis was performed to measure the thermal lesion detectability of MR images. A ROI was defined in the thermal lesion and another ROI with the same geometry and size was defined in the normal tissue to calculate various image quality metrics including lesion contrast, lesion SNR, tissue SNR, and lateral and axial spatial resolutions [22].

Lesion contrast is given by the equation:

$$lC = (I_{lesion} - I_{tissue}) / I_{tissue} \tag{2}$$

where I_{lesion} and I_{tissue} represent the average signal intensities, i.e., MRI image pixel intensities, of the thermal lesion and the normal

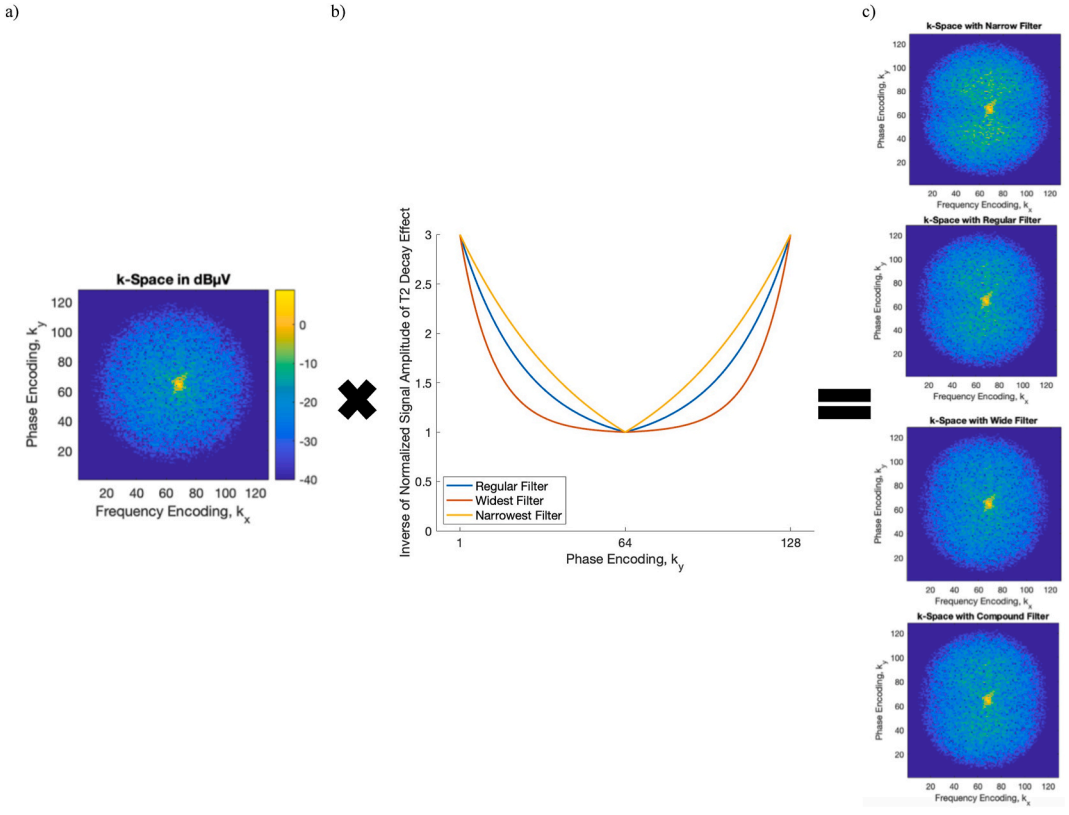

Fig. 3. Inverse filter at various widths and the resultant k-space. In the inverse Fourier transform (IFT) multiplication scheme, (a) the original k-space is multiplied with (b) various inverse filters to reduce the effects of T2 decay in the phase-encoding direction of k-space where (c) is the resultant k-space after the multiplication of the respective widths of the inverse filters.

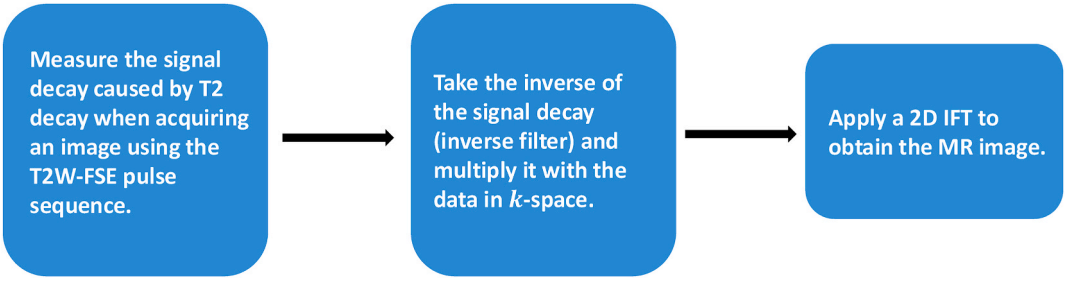

Fig. 4. Flowchart of the inverse Fourier transform (IFT) multiplication scheme. The scheme compensates for signal decay by calculating an inverse filter based on the decay and multiplying it to the *k*-space. A 2D inverse Fourier transform is then applied to reconstruct the final enhanced MR image, improving image quality by mitigating the effects of T2 decay.

tissue within the ROI, respectively [23].

Lesion SNR is a simplified image quality metric to assess the detectability of a target (e.g., a HIFU thermal lesion) given by:

$$lSNR = lC \cdot tSNR \cdot \sqrt{\frac{A_l}{SR_{lateral} \cdot SR_{axial}}} \tag{3}$$

where $tSNR = I_{tissue}/\sigma_{tissue}$ represents tissue SNR, and I_{tissue} and σ_{tissue} are the average and standard deviation of the signal intensity of the normal tissue within the ROI, respectively [23]. A_l, the lesion area, was given a fixed value of 2.25 mm^2 (1.5 mm $\times$ 1.5 mm). A conservative value was chosen because the induced HIFU thermal lesion makes up 2–3 mm of a given 6 mm tissue sample. This fixed area ensured that A_l only consisted of HIFU thermal lesion for a given sample and the size of the ROI defined in the normal tissue was also given the same fixed area of 2.25 mm^2 (1.5 mm $\times$ 1.5 mm). The spatial resolutions in the lateral and axial directions ($SR_{lateral}$ and SR_{axial}) are determined using the full width at half maximum (FWHM) of the line spread function (LSF) in the respective direction. LSF is derivative of the edge spread function (ESF), which is an acquisition of the signal intensity along a high contrast edge [24,25]. Finally, the quantitative image analysis results of the enhanced MR images were compared to the original T2W-FSE MR image to determine the improvement in the detection of HIFU thermal lesions.

3. Results

3.1. HIFU heating of ex vivo porcine muscle tissue

HIFU acoustic power of 24.6 W was focused into an *ex vivo* porcine muscle tissue sample, which was later bisected to reveal coagulated tissue at the HIFU focal point (Fig. 5). During HIFU heating, the affected tissue reached a cytotoxic temperature that led to protein denaturation and coagulative necrosis, thereby causing a color change from pink to white [8,26-28]. In addition, the structural changes caused by protein denaturation, and the tissue dehydration caused by rising tissue temperature, collectively stiffened the coagulated tissue [8,29].

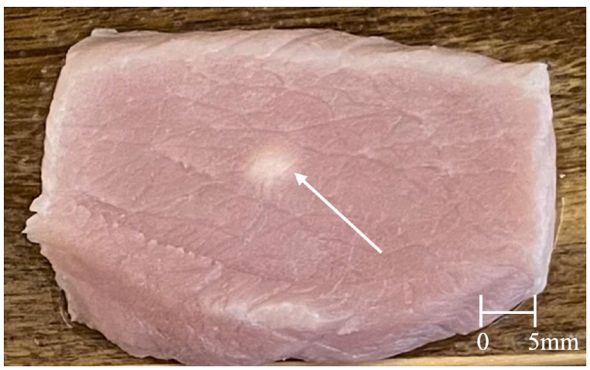

Fig. 5. An *ex vivo* porcine muscle tissue sample was exposed to a high intensity focused ultrasound (HIFU) acoustic power of 24.6 W for 30 s. A white circular cross-section corresponding approximately to the diameter of the HIFU focal point in the centre of a mostly homogeneous tissue sample is a HIFU thermal lesion with a diameter of 4 mm (arrow).

3.2. T2W-FSE MR image acquisition of ex vivo porcine muscle tissue

Prepared tissue samples were imaged using the T2W-FSE pulse sequence with the benchtop MRI research system. The MR images consist of a hyperintense normal tissue and a hypointense thermal lesion (Fig. 6). Thermal lesions appear hypointense in MR images because the T2 relaxation time is linearly proportional to water content [30]. Coagulative necrosis, which leads to the creation of thermal lesions, involves the denaturation of proteins and tissue dehydration [31]. Therefore, the coagulated tissues have a lower water content than normal tissue and consequently, shorter T2 relaxation time, thereby appearing hypointense in T2W-FSE MR images [9,32,33]. Fig. 6a shows the original T2W-FSE MR image of one of the four prepared tissue samples. Fig. 6c–f presents enhanced MR images using the regular, wide, narrow, and compound inverse filters, respectively. Image quality metrics – lesion contrast, lesion SNR, tissue SNR, and spatial resolutions – were calculated for these images.

3.3. Quantitative image analysis

Quantitative analysis of the image quality metrics of the original and enhanced MR images will determine the extent to which the various inverse filters improve the MR images. Specifically, this analysis quantifies the lateral and axial spatial resolutions, lesion contrast, tissue SNR, and lesion SNR. The percentage improvements in these image quality metrics of the enhanced MR images were compared to those of the original MR images, and the significance of each improvement was evaluated using the *t*-test statistical analysis. The analysis was conducted using four tissue samples, and the results reported are the average improvements across these four samples. Furthermore, a one-way analysis of variance (ANOVA) was performed to determine if there is a statistically significant difference between the image quality metrics of enhanced MR images using the various filters.

3.3.1. Spatial resolution

The spatial resolution of an MR image is determined by plotting the signal intensities along a high contrast edge (Fig. 7a), calculating their spatial derivative along the edge (Fig. 7b), and finally measuring the FWHM of the spatial derivative (Fig. 7c). For all MR images, the FWHM calculated in the lateral and axial directions represents the lateral and axial spatial resolutions. All four filters showed significant improvements ($p < 0.05$) in the lateral and spatial resolutions of the enhanced MR images, where the narrow filter yielding the largest improvements of 13.8 ± 2.5 % and 17.0± 2.3 %, respectively (Fig. 8). This noticeable improvement indicates that

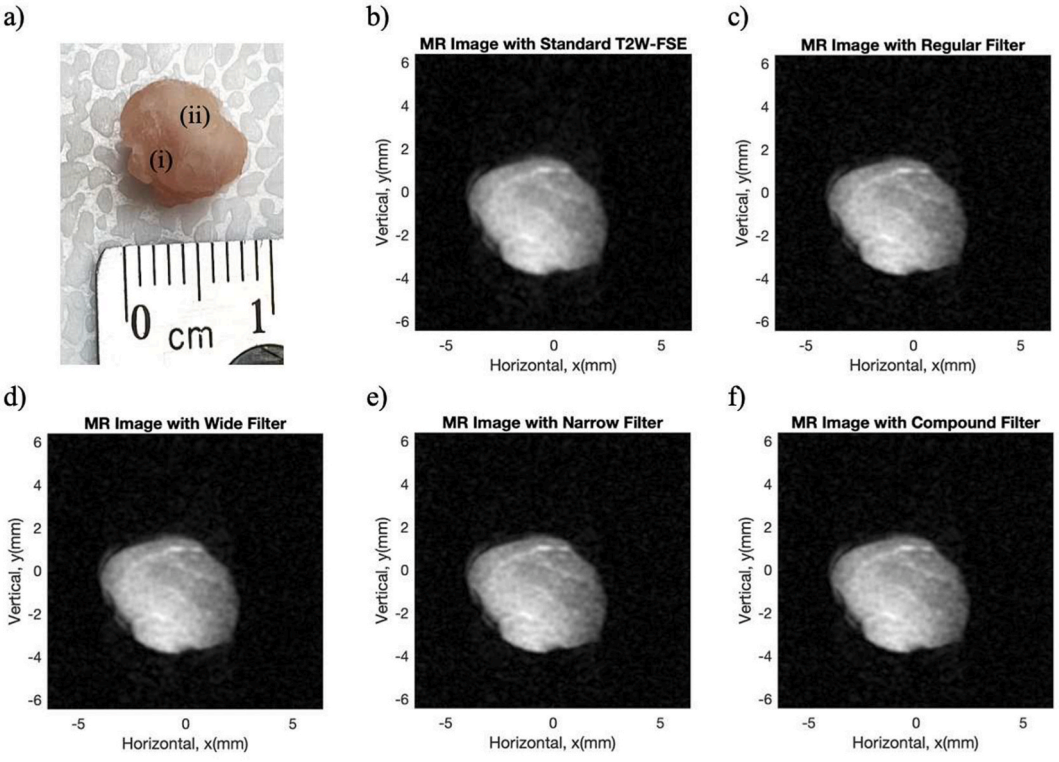

Fig. 6. One of four data sets of tissue sample with high intensity focused ultrasound (HIFU) induced thermal lesion. (a) Photograph of tissue sample where (i) is normal tissue and (ii) is thermal lesion. (b) Original T2-weighted fast spin echo (T2W-FSE) MR image, and enhanced MR images using the (c) regular, (d) wide, (e) narrow, and (f) compound inverse filters where normal tissue appear hyperintense and thermal lesion appear hypointense.

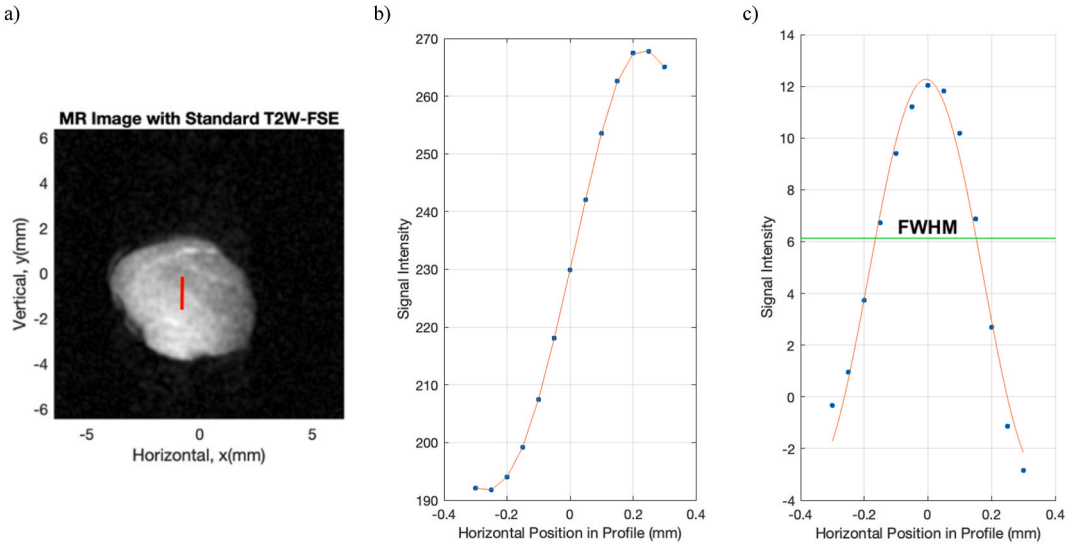

Fig. 7. Calculation of axial spatial resolution of original MR image. (a) The signal intensity is acquired along a high contrast edge of the image (red line – not to scale) to acquire (b) an edge spread function (ESF), and (c) its derivative, the line spread function (LSF), whose full width at half maximum (FWHM) (green line) is the axial spatial resolution of the MR image.

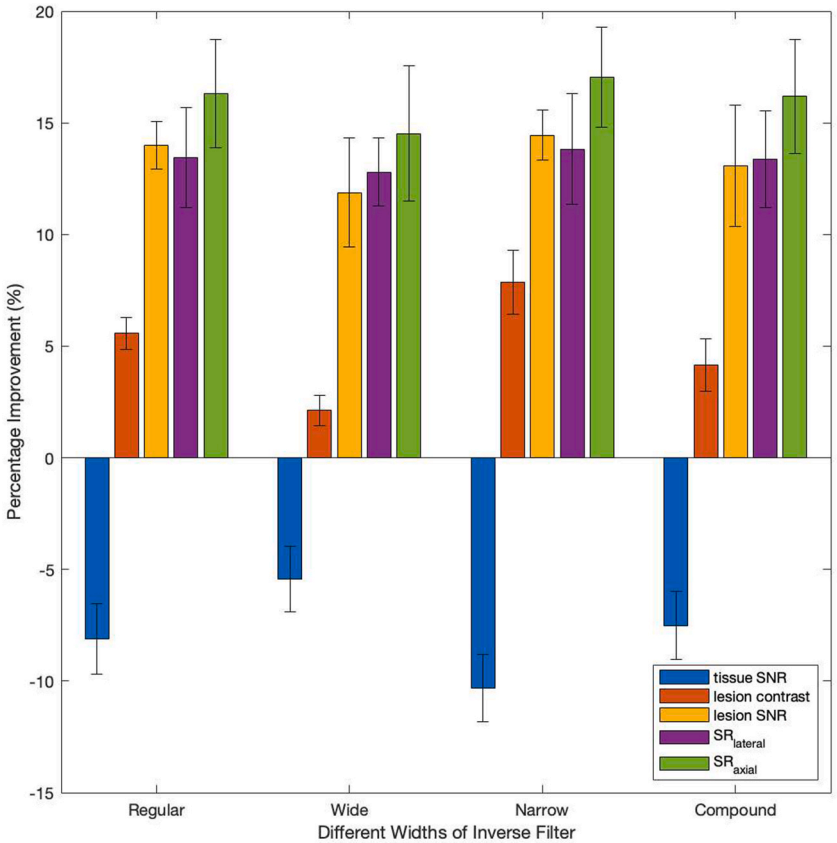

Fig. 8. Summary of percentage improvement of four tissue samples with high intensity focused ultrasound (HIFU) induced thermal lesion. Average and standard deviation of percentage improvement of image quality metrics of lesion contrast, lesion signal-to-noise ratio (SNR), lateral and axial spatial resolution, and tissue SNR of enhanced MR images compared to the original T2-weighted fast spin echo (T2W-FSE) MR image have been calculated.

the exponential signal loss caused by T2 decay, which results in a loss of spatial resolution, is compensated by the inverse filter. Furthermore, the upper limit of the range of the filter, which is multiplied to the periphery of *k*-space, amplifies the signals of the high spatial frequencies responsible for determining the spatial resolutions of MR images [20]. However, one-way ANOVA showed that there was no statistically significant difference between the improvements provided by the different filters ($p > 0.05$).

3.3.2. Lesion contrast

Lesion contrast of MR images was determined by taking the difference of the average signal intensity of the thermal lesion and the normal tissue within the ROI over the average intensity of the normal tissue within the ROI (Equation (2)). The lesion contrasts of enhanced MR images using the regular, wide, narrow, and compound inverse filters were comparable to the original T2W-FSE MR image (Fig. 8) and to each other, with no statistically significant differences observed ($p > 0.05$). This was expected because the lower limit of the range of the filter was purposely set to 1, ensuring that the signal in the centre of *k*-space, responsible for contrast of MR images, remains unaffected [20].

3.3.3. Tissue signal-to-noise ratio (tSNR) and lesion signal-to-noise ratio (lSNR)

Tissue SNR (*tSNR*) is an image quality metric used to calculate lesion SNR (*lSNR*) (Equation (3)). Compared with the original T2W-FSE MR image, enhanced MR images had significantly lower calculated *tSNR* values of $p < 0.05$ with the narrow filter yielding the largest average reduction of -10.3 ± 1.5 % (Fig. 8). The loss in *tSNR* is inevitable because the inverse filter is applied to both the signal and the noise present in *k*-space, whereas the T2 decay only affects the signal in *k*-space. Therefore, there is an inherent trade-off between *tSNR* and spatial resolutions because *tSNR* decreases with smaller lateral and axial spatial resolutions. Although *tSNR* is proportional to *lSNR*, we found that enhanced MR images had significantly higher *lSNR* values ($p < 0.05$) compared to that of the original MR image. Specifically, the MR image enhanced with the narrow filter yielded the largest average *lSNR* increase of 14.4 ± 1.1% (Fig. 8). Lesion SNR improved because it depends on lesion contrast, spatial resolutions, and tissue SNR (Equation (3)). Therefore, *tSNR* reduction was more than offset by higher lesion contrast and smaller lateral and axial spatial resolutions, yielding a net increase in *lSNR* [15]. However, the differences in both *tSNR* and *lSNR* across the various filters were not statistically significant ($p > 0.05$).

4. Discussion

Compared to the original T2W-FSE MR image of normal and coagulated tissues, MR images enhanced using inverse filters showed improved image quality metrics, whose percentage improvements represent average values of high contrast areas across different tissue samples. T-test analyses evaluated the significance of the improvements, where the enhanced MR images exhibited: 1) higher lesion SNR, 2) lower tissue SNR, 3) smaller lateral and axial spatial resolutions, and 4) comparable lesion contrast. However, when comparing the performance of the filters themselves, the differences were not statistically significant ($p > 0.05$), indicating that no single filter was significantly better than the others. Despite this, it is worth noting that the narrow filter exhibited the highest percentage improvements in several metrics, suggesting that it may provide slightly better results.

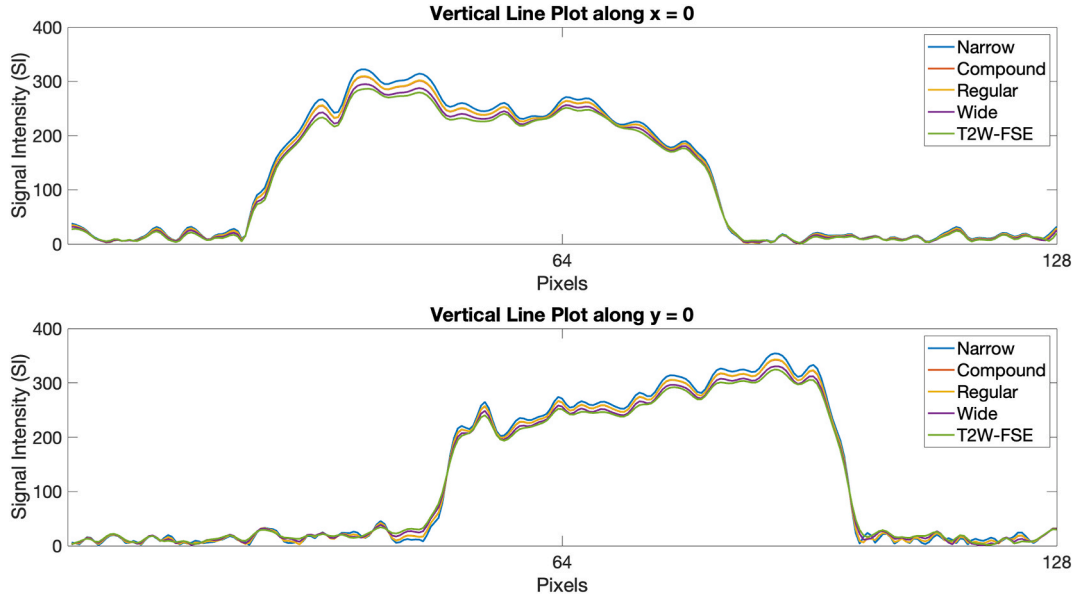

Fig. 9. Horizontal line plots (top, along $y = 0$) and vertical line plots (bottom, along $x = 0$) of one tissue sample illustrate differences in signal intensity between the original and enhanced MR image. The highest signal intensity is observed in enhanced MR images using the narrow filter, followed by regular, compound, and wide filters. All four tissue samples exhibited the same trend in their respective line plots.

The improvement in image quality metrics for enhanced MR images with the regular filter indicates that the T2 decay has been effectively compensated for through the application of the inverse filter to the phase encoding direction of *k*-space.

The compounding filter was intended to reduce speckle noise in the images [21]. However, the image quality metrics for enhanced MR images with this filter yielded lower values compared to those obtained with the regular filter. The limited improvement observed with the compound filter is likely because the compounding technique is more commonly utilized in ultrasound images [34]. Furthermore, the width of the compounding filter was similar to that of the regular filter, resulting in comparable results for the MR images with both filters. This observation is consistent with Fig. 3, which illustrates that the *k*-space with the application of the compound filter is comparable to that of the *k*-space with the application of the regular filter.

MR images with the narrow filter exhibit the most noticeable improvement, likely due to the multiplication of a larger area under the narrow filter compared to the regular filter. This results in more amplification of signals in *k*-space. Therefore, the narrow filter not only amplifies the signals in *k*-space, but also effectively eliminates the signal modulation in *k*-space caused by the T2 decay. This was expected because the signals amplified the most, especially in the periphery of *k*-space, when the narrow filter was implemented (Fig. 3).

On the other hand, the wide filter has the smallest area under the inverse filter and consequently, a smaller area of signal amplification in *k*-space (Fig. 3). This results in an ineffective compensation for the exponential signal modulation in *k*-space caused by the T2 decay. As a result, MR images with the wide filter showed the least improvement in image quality metrics.

These findings are further supported by the line plots, acquired along the horizontal and vertical axes of the MR images. Fig. 9 depicts horizontal and vertical line plots of one tissue sample, but the same trend was observed for all tissue samples with the largest signal intensities occurring in the enhanced MR images with the narrow filter followed by regular, compound, and wide filters. It is important to note that the line plot of the compound filter is not visible due to its close proximity to the line plot of the regular filter. These line plots correlate to the percentage improvement of the image quality metrics, as the average and the standard deviation of the signal intensity in the ROI of the thermal lesion and the normal tissue were used to calculate the image quality metrics with the narrow filter showing the most improvement followed by regular, compound, and wide filters.

The main limitation of our developed methodology is that only three filter widths ($\beta = 0.5, 1,$ and 2) were considered. Furthermore, our study was limited by the small tissue size (6–7 mm diameter) requirement and a relatively low magnetic field strength of 0.55 T of the research MRI scanner. These limitations necessitated the cutting of tissue samples into small dimensions and resulted in a weaker SNR, respectively. Implementing the method in a clinical MRI with a typical static magnetic field strength of 1.5 T–3 T would allow imaging of larger tissue samples with clinically relevant dimensions, yielding a larger SNR and allowing an overall further improvement in image quality. Additionally, this method could be further investigated with MR imaging at higher acoustic power of HIFU, making it more clinically relevant and potentially useful for clinical application. Finally, thermal diffusion is another factor that was not accounted for in our study. The heat can spread beyond the focal point, leading to a gradual transition rather than a clear boundary between the treated and untreated tissues [35]. This diffusion can be monitored in real-time using MR thermometry, which allows for precise temperature mapping around the treated area [36]. A future study could involve implementing our methodology with MR thermometry to investigate whether this provides an improvement in defining treatment boundaries.

5. Conclusion

In summary, the optimal choice for effectively addressing T2 decay in correcting the exponential decay of signals in the phase-encoding direction of *k*-space appears to be the utilization of the inverse of the signal modulation. Specifically, our results demonstrate that, among the filters studied in this work, the narrow inverse filter best amplifies the signals and eliminates the exponential signal modulation in *k*-space caused by the T2 decay, leading to the largest improvements in image quality metrics and consequently, in thermal lesion detectability. This suggests the potential translation of the IFT multiplication scheme to the clinic as a method to enhance the detection of thermal lesions in MR-guided HIFU procedures.

CRediT authorship contribution statement

Gabrielle S. Lee: Writing – review & editing, Writing – original draft, Visualization, Validation, Software, Project administration, Methodology, Investigation, Formal analysis, Data curation, Conceptualization. **Graham A. Ferrier:** Writing – review & editing, Resources. **Jahangir (Jahan) Tavakkoli:** Writing – review & editing, Supervision, Funding acquisition, Conceptualization.

Data availability statement

Data have been deposited at Mendeley Data (https://data.mendeley.com/datasets/ntfg5hdbch/1) with accession number 10.17632/ntfg5hdbch.1.

Funding

This work was funded by Natural Sciences and Engineering Research Council of Canada (NSERC) Discovery and Mitacs grants that were awarded to J. Tavakkoli.

Declaration of competing interest

The authors declare that they have no known competing financial interests or personal relationships that could have appeared to influence the work reported in this paper.

Acknowledgments

The authors would like to thank Professors Yuan Xu and Miranda Kirby from the Department of Physics at Toronto Metropolitan University for their helpful suggestions and discussions. We would also like to thank Markus Muetzel from Pure Devices for their technical assistance, specifically with the OpenMATLAB interface of the research MRI scanner. The authors also thank the anonymous reviewers for their valuable comments and suggestions.

References

[1] Health Promotion and Chronic Disease Prevention in Canada, Canadian cancer statistics 2021, Health Promot Chronic Dis Prev Can 41 (11) (2021) 399, https://doi.org/10.24095/hpcdp.41.11.09.
[2] K. Haume, S. Rosa, S. Grellet, M. Smialek, K. Butterworth, A. Solov'yov, K. Prise, J. Golding, N. Mason, Gold nanoparticles for cancer radiotherapy: a review, Cancer Nanotechnol 7 (1) (2016) 1–20, https://doi.org/10.1186/s12645-016-0021-x.
[3] I. Mellal, A. Oukaira, E. Kengne, A. Lakhssassi, Thermal therapy modalities for cancer treatment: a review and future perspectives, Int. J. Agric. Sci. Res. 4 (2) (2017) 1–11, https://doi.org/10.21767/2394-9988.100064.
[4] R. Habash, R. Bansal, D. Krewski, H. Alhafid, Thermal therapy, Part 1: an introduction to thermal therapy, Crit. Rev. Biomed. Eng. 34 (6) (2006) 459–489, https://doi.org/10.1615/critrevbiomedeng.v34.i6.20.
[5] I. Elhelf, H. Albahar, U. Shah, A. Oto, E. Cressman, M. Almekkawy, High intensity focused ultrasound: the fundamentals, clinical applications and research trends, Diagn Interv Imaging 99 (6) (2018) 349–359, https://doi.org/10.1016/j.diii.2018.03.001.
[6] C. Diederich, Thermal ablation and high-temperature thermal therapy: overview of technology and clinical implementation, Int. J. Hyperther. 21 (8) (2005) 745–753, https://doi.org/10.1080/02656730500271692.
[7] J. Jacobson, Musculoskeletal ultrasound: focused impact on MRI, Am. J. Roentgenol. 193 (3) (2009) 619–627, https://doi.org/10.2214/AJR.09.2841.
[8] F. Jolesz, MRI-guided focused ultrasound surgery, Annu. Rev. Med. 60 (2009) 417–430, https://doi.org/10.1146/annurev.med.60.041707.170303.
[9] L. Chen, D. Bouley, E. Yuh, H. D'Arceuil, K. Butts, Study of focused ultrasound tissue damage using MRI and histology, J. Magn. Reson. Imag. 10 (2) (1999) 146–153, https://doi.org/10.1002/(sici)1522-2586(199908)10:2<146::aid-jmri6>3.0.co;2-c.
[10] J. Hennig, M. Weigel, K. Scheffler, Multiecho sequences with variable refocusing flip angles: optimization of signal behavior using smooth transitions between pseudo steady states (TRAPS), Magn. Reson. Med. 49 (3) (2003) 527–535, https://doi.org/10.1002/mrm.10391.
[11] P. Keller, J. Heiserman, E. Fram, S. Rand, B. Drayer, A Nyquist modulated echo-to-view mapping scheme for fast spin-echo imaging, Magn. Reson. Med. 33 (6) (1995) 838–842, https://doi.org/10.1002/mrm.
[12] M. Bernstein, K. King, X. Zhou, Handbook of MRI Pulse Sequences, Academic Press, Cambridge, 2004.
[13] D. Chien, R. Mulkern, Fast spin-echo studies of contrast and small-lesion definition in a liver-metastasis phantom, J. Magn. Reson. Imag. 2 (4) (1992) 483–487, https://doi.org/10.1002/jmri.1880020419.
[14] X. Zhou, G. Cofer, S. Suddarth, G. Johnson, High-field MR microscopy using fast spin-echo pulse sequences, Magn. Reson. Med. 30 (1) (1993) 60–67, https://doi.org/10.1002/mrm.1910300110.
[15] X. Zhou, Z. Liang, G. Cofer, C. Beaulieu, S. Suddarth, G. Johnson, Reduction of ringing and blurring artifacts in fast spin-echo imaging, J. Magn. Reson. Imag. 3 (5) (1993) 803–807, https://doi.org/10.1002/jmri.
[16] R. Mulkern, S. Wong, C. Winalski, F. Jolesz, Contrast manipulation and artifact assessment of 2D and 3D RARE sequences, Magn. Reson. Imaging 8 (5) (1990) 557–566, https://doi.org/10.1016/0730-725x(90)90132-l.
[17] S. Friis, T. Hansen, M. Poulsen, H. Gregersen, A. Bruel, J. Vinge Nygaard, Biomechanical properties of the stomach: a comprehensive comparative analysis of human and porcine gastric tissue, J. Mech. Behav. Biomed. Mater. 138 (2023) 105614, https://doi.org/10.1016/j.jmbbm.2022.105614.
[18] R. Siavash, J. Tavakkoli, An acoustic backscatter-based method for estimating attenuation towards monitoring lesion formation in high intensity focused ultrasound, AIP Conf. Proc. 1503 (1) (2012) 107–112, https://doi.org/10.1063/1.4769926.
[19] R. Bitar, G. Leung, R. Perng, S. Tadros, A. Moody, J. Sarrazin, C. McGregor, M. Christakis, S. Symons, A. Nelson, T. Roberts, MR pulse sequences: what every radiologist wants to know but is afraid to ask, Radiographics 26 (2) (2006) 513–537, https://doi.org/10.1148/rg.262055063.
[20] C. Paschal, H. Morris, K-space in the clinic, J. Magn. Reson. Imag. 19 (2) (2004) 145–159, https://doi.org/10.1002/jmri.10451.
[21] C. Lin, Y. Sun, C. Lin, A motion compounding technique for speckle reduction in ultrasound images, J. Digit. Imag. 23 (3) (2010) 246–257, https://doi.org/10.1007/s10278-008-9172-6.
[22] J. Bushberg, The Essential Physics of Medical Imaging, Lippincott Williams & Wilkins, Philadelphia, 2012.
[23] N. Zhao, Y. Xu, Decorrelated compounding improves lesion signal-to-noise ratio of low-contrast lesions in synthetic transmit aperture ultrasound imaging, JASA Express Lett 2 (2) (2022) 1–8, https://doi.org/10.1121/10.0009385.
[24] A. Webb, Introduction to Biomedical Imaging, John Wiley & Sons, Hoboken, 2003.
[25] K. Kohm, Modulation transfer function measurement method and results for the Orbview-3 high resolution imaging satellite, Int. Arch. Photogram. Rem. Sens. Spatial Inf. Sci. 35 (2004) 1–6.
[26] S. Goldberg, G. Gazelle, P. Mueller, Thermal ablation therapy for focal malignancy: a unified approach to underlying principles, techniques, and diagnostic imaging guidance, Am. J. Roentgenol. 174 (2) (2000) 323–331.
[27] S. Hectors, I. Jacobs, C. Moonen, G. Strijkers, K. Nicolay, MRI methods for the evaluation of high intensity focused ultrasound tumor treatment: current status and future needs, Magn. Reson. Med. 75 (1) (2016) 302–317, https://doi.org/10.1002/mrm.25758.
[28] C. Janko, L. Munoz, R. Chaurio, C. Maueroder, C. Berens, K. Lauber, M. Herrmann, Navigation to the graveyard-induction of various pathways of necrosis and their classification by flow cytometry, Methods Mol. Biol. 1004 (2013) 3–15, https://doi.org/10.1007/978-1-62703-383-1_1.
[29] J. Biederer, M. Beer, W. Hirsch, J. Wild, M. Fabel, M. Puderbach, E. Van Beek, MRI of the lung (2/3). Why … when … how? Insights Imaging 3 (4) (2012) 355–371, https://doi.org/10.1007/s13244-011-0146-8.
[30] L. Liu, B. Yin, K. Shek, D. Geng, Y. Lu, J. Wen, X. Kuai, W. Peng, Role of quantitative analysis of T2 relaxation time in differentiating benign from malignant breast lesions, J. Int. Med. Res. 46 (5) (2018) 1928–1935, https://doi.org/10.1177/0300060517721071.
[31] L. Wilkins, Monitoring liver stiffness changes during controlled hyperthermia and microwave ablation using point shear-wave elastography, Radiol Imaging Cancer 1 (2) (2019) e194013, https://doi.org/10.1148/rycan.2019194013.
[32] C. Damianou, K. Ioannides, V. Hadjisavvas, N. Mylonas, A. Couppis, D. Iosif, P. Kyriacou, MRI monitoring of lesions created at temperature below the boiling point and of lesions created above the boiling point using high intensity focused ultrasound, J. Bio. Sci. 3 (2010) 1–13, https://doi.org/10.4236/jbise.2010.38102.
[33] L. Curvo-Semedo, J. Brito, M. Seco, J. Costa, C. Marques, F. Caseiro-Alves, The hypointense liver lesion on T2-weighted MR images and what it means, Radiographics 30 (1) (2010) 1–24, https://doi.org/10.1148/rg.e38.

[34] C. Lin, C. Weng, Y. Sun, Ultrasound image compounding based on motion compensation, Conf Proc IEEE Eng Med Biol Soc (2005) 6445–6448, https://doi.org/10.1109/IEMBS.2005.1615974.
[35] L. Yeshurun, L. Azahri, Non-invasive measurement of thermal diffusivity using high-intensity focused ultrasound and through-transmission ultrasonic imaging, Ultrasound Med. Biol. 42 (1) (2016) 243–256, https://doi.org/10.1016/j.ultrasmedbio.2015.09.004.
[36] R. Mattay, K. Kim, L. Shah, B. Shah, L. Sugrue, F. Safoora, E. Ozhinsky, K. Narsinh, MR thermometry during transcranial MR imaging–guided focused ultrasound procedures: a review, AJNR Am J Neuroradiol 45 (1) (2023) 1–8, https://doi.org/10.3174/ajnr.A8038.